How nanopore translocation experiments can measure RNA unfolding

Prasad Bandarkar¹, Huan Yang¹, Robert. Y. Henley², Meni Wanunu¹, Paul C. Whitford¹

¹Department of Physics, Northeastern University, Boston MA, ²Genomic Analysis Laboratory, The Salk Institute for Biological Studies, La Jolla, CA

Abstract

Electrokinetic translocation of biomolecules through solid-state nanopores represents a label-free single-molecule technique that may be used to measure biomolecular structure and dynamics. Recent investigations have attempted to distinguish individual transfer RNA (tRNA) species based on the associated pore translocation times, ion-current noise and blockage currents. By manufacturing sufficiently small pores, each tRNA is required to undergo a deformation in order to translocate. Accordingly, differences in nanopore translocation times/distributions may be used to infer the mechanical properties of individual tRNA molecules. In order to bridge our understanding of tRNA structural dynamics and nanopore measurements, we apply molecular dynamics (MD) simulations using a simplified "structure-based" energetic model. Calculating the free-energy landscape for distinct tRNA species implicates transient unfolding of the terminal RNA helix during nanopore translocation. This provides a structural/energetic framework for interpreting current experiments, which can aid the design of methods for identifying macromolecules using nanopores.

Received for publication Date and in final form Date.

p.whitford@neu.edu,m.wanunu@northeastern.edu

Statement of significance

The current study employs simulations to explore the structural characteristics that govern transport of tRNA through a nanopore. By adopting a simplified description, the presented calculations demonstrate that the energetics of tRNA folding can rationalize the differential translocation timescales that have been observed in experiments. Through comparison with experimental measurements, the presented calculations provide a physical-chemical foundation that can enable nanopore technologies to measure the stabilities of RNA helices.

Introduction

Advances in nanopore fabrication and design (1-5) provide a range of new opportunities to probe the physical characteristics of biomolecules. In nanopore experiments, a dielectric membrane with a single nanopore separates two electrodes in an electrolytic cell, and charged biomolecules are introduced into one of the chambers. When a voltage is applied between the electrodes, the flow of ions results in a constant "open-pore" current. However, when a biomolecule reaches the pore opening, the flow of ions is partially (or fully) obstructed. This results in a net reduction of the current flow, where the duration and current level depends on the properties of the biomolecule. To quantify blockage dynamics, the most commonly employed metrics are the magnitude (ΔI) and duration (dwell time, t_d) of the current drop. Since these quantities are sensitive to the precise physical attributes of the pore-biomolecule complex, the statistical properties of blockage distributions will encode signatures of the biomolecular dynamics.

Quantifying transport through nanopores has the potential to provide insights into the physical properties that govern functional dynamics of biomolecules, such as proteins (6–10) and transfer RNA (tRNA) (11, 12). During protein synthesis in the cell, codon-anticodon interactions are formed between tRNA and messenger RNA (mRNA), which allow the ribosome to accurately decode mRNA sequences. Since the energetic differences between correct and incorrect tRNA base-pairing can only partially account for the fidelity of translation, the ribosome employs a subsequent proofreading step (13–15). This involves a large-scale conformational change (i.e. accommodation) in the incoming tRNA molecule, where intramolecular

© 2013 The Authors 0006-3495/08/09/2624/12 \$2.00

doi: XXX/XXX

tRNA interactions that are distal to the anticodon region can modulate the accuracy of translation (16). Subsequent to accommodation, tRNA molecules must undergo several additional rearrangements in order to complete the elongation cycle (17–20), and a balance between ribosome and tRNA flexibility is necessary to ensure rapid dynamics (21–23). With the essential role of molecular flexibility during protein synthesis, measuring the mechanical properties of tRNA can help reveal principles that underlie accurate gene expression. Accordingly, this class of molecules represents an excellent test case for the application of nanopore-based measures of molecular flexibility, where physical insights can have biological implications.

In recent nanopore translocation experiments it was shown that current signals for different tRNA species are sufficiently distinct that one may differentiate the tRNA species. By combining the signals with machine-learning algorithms, the identity of one type of tRNA in a binary mixture could also be discerned from a single-molecule pulse (12). In those experiments, the width of the nanopore was chosen to be larger than the radius of an RNA double helix, while also sufficiently small that a tRNA is unable to translocate without undergoing a deformation (Fig. 1). The motivation for the measurement was, since the molecule must rearrange in order to translocate, it could be possible to use nanopores to measure molecular flexibility. These early experiments demonstrated a potential for nanopores to elucidate the mechanical properties of RNA, where future objectives may include the characterization of mutations, as well as post-transcriptional modifications. However, while structural data suggests qualitative mechanistic interpretations, establishing a quantitative relationship between current changes and biomolecular properties will require a more comprehensive physical-chemical framework. It is our expectation that a detailed understanding of this relationship may allow next-generation nanopore measurements to provide precise insights into biologically-relevant molecular properties.

In the current study, we employ molecular dynamics simulations (MD) with a simplified model of tRNA to explore the relationship between structural dynamics and nanopore translocation kinetics. Here, we describe the internal energetics of the tRNA molecule using a force field in which all non-hydrogen atoms are represented and the native conformation is explicitly defined to be stable (i.e. an all-atom structure based model (24, 25)). To mimic the pore, we account for excluded volume interactions between the pore and tRNA, where electrophoretic effects are treated through perturbative techniques. While this is intended to be a simplified representation, we find that it is sufficient to capture the experimentally-observed differential kinetics of tRNA species. Contrary to expectations, this analysis also indicates that the translocation process is not associated with simple bending/shearing motions of the tRNA. Rather, there is a dramatic unfolding of the tRNA acceptor arm helix. Taken together, these results illustrate how current nanopore technologies may be combined with molecular simulations to measure the stabilities of individual helices within RNA assemblies.

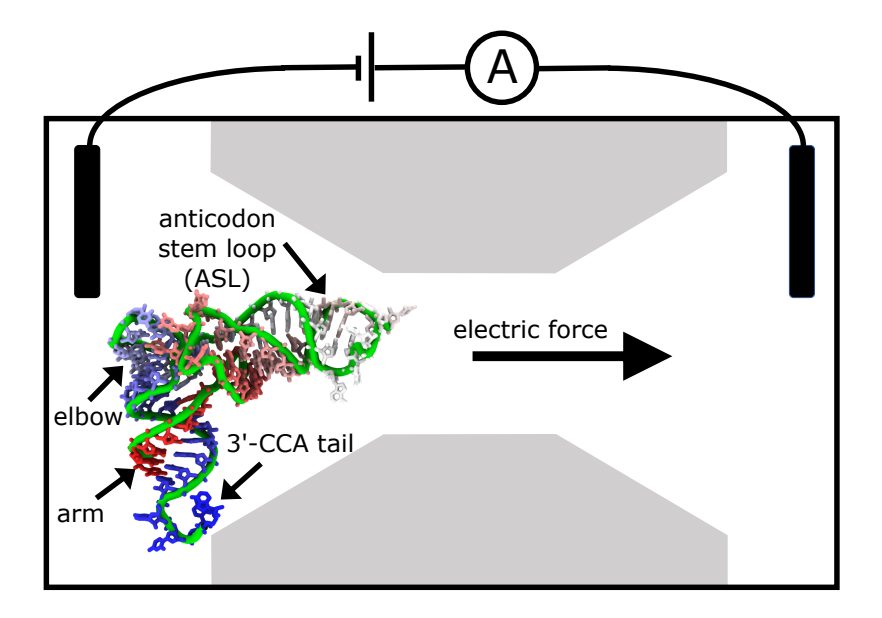


Figure 1: Schematic representation of a tRNA-nanopore experiment. A dielectric membrane (gray) separates the electrolytic cell into two chambers, where solvent is allowed to pass through a nanometer-scale pore. The geometry of a nanopore typically consists of conical openings connected by a cylindrical region. Here, the diameter of the cylinder is drawn to-scale, relative to the dimensions of a tRNA molecule. Due to the L-shaped structure of a tRNA molecule, translocation through a nanopore requires molecular deformations, which may involve a range of distortions. The detailed character of these deformations will govern the measured changes in ion currents.

Methods

RNA Force Field

An all-atom structure-based model (24) was used to describe the intramolecular energetics of the tRNA molecule. This model was generated using the SMOG-server webtool (25). In this model, all heavy (non-Hydrogen) atoms are represented as spheres of unit mass. The functional form of the potential is given by

$$V = \sum_{\text{bonds}} \epsilon_r (r - r_0)^2 + \sum_{\text{angles}} \epsilon_{\theta} (\theta - \theta_0)^2$$

$$+ \sum_{\text{improper and planar} \atop \text{dihedrals}} \epsilon_{\chi} (\chi - \chi_0)^2 + \sum_{\text{flexible} \atop \text{dihedrals}} \epsilon_{\phi} F(\phi, \phi_0)$$

$$+ \sum_{\text{contacts}} \epsilon_c \left[\left(\frac{\sigma_{ij}}{r_{ij}} \right)^{12} - 2 \left(\frac{\sigma_{ij}}{r_{ij}} \right)^6 \right] + \sum_{\text{non-contacts}} \epsilon_{nc} \left(\frac{\sigma_{NC}}{r_{ij}} \right)^{12}$$

$$(1)$$

where

$$F(\phi) = [1 - \cos(\phi - \phi_0)] + \frac{1}{2} [1 - \cos(3(\phi - \phi_0))]. \tag{2}$$

The parameters $\{r_0\}$, $\{\theta_0\}$, $\{\chi_0\}$, $\{\phi_0\}$ and $\{\sigma_{ij}\}$ are given the values adopted in the crystallographic structure of each molecule. Thus, the potential energy is defined to have a global minimum that corresponds to the crystallographic structure. We use a reduced energy scale in units of $\epsilon_0=1$ for all terms. As described below, free-energy profiles were calculated at a reduced temperature of 0.71. Accordingly, $\epsilon_0=\frac{k_BT}{0.71}=1.42k_BT$. Consistent with previous implementations, the coefficients for this model are given the values $\epsilon_r=50\epsilon_0/\text{nm}^2$, $\epsilon_\theta=40\epsilon_0/\text{rad}^2$, $\epsilon_{\chi improper}=10\epsilon_0/\text{rad}^2$, $\epsilon_{\chi planar}=40\epsilon_0/\text{rad}^2$, $\epsilon_{NC}=0.01\epsilon_0$ and $\sigma_{NC}=2.5\text{Å}$. To assign the dihedral strengths, the number of dihedral angles that share a pair of atoms is determined. If N_D is the number of dihedrals shared by a bond, the energy of each such dihedral angle is scaled by $1/N_D$. The weights of the dihedral and contact energies are set such that

$$\frac{\sum \epsilon_c}{\sum \epsilon_\phi} = 2 \text{ and}$$

$$\sum \epsilon_c + \sum \epsilon_\phi = N\epsilon_0$$
(3)

where N is the number of atoms in the molecule.

As seen in the functional form of the potential, all the interactions (except for non-contacts) stabilize the crystallographic structure of the molecule. By defining an experimental structure as stable, the direct interactions in this model describe the effective energetics of the system. That is, each stabilizing non-bonded term implicitly accounts for the stability imparted by non-specific electrostatic and solvent interactions. The non-contacting atom pairs are given excluded volume interactions, which ensure that proper stereochemistry is preserved. The structures were obtained from PDB entries 1F7U (26) for tRNA Arg, 1QU3 (27) for tRNA le and 1EHZ(28) for tRNA Phe.

tRNA-pore interaction

In the presented model, the tRNA only interacts with the pore through an excluded volume interaction:

$$V_{\text{pore}} = \sum_{\text{all atoms}} \epsilon_{pore} \left(\frac{\sigma_{\text{pore}}}{r}\right)^{12},\tag{4}$$

where $\epsilon_{\text{pore}} = \epsilon_{\text{NC}} = 0.01\epsilon_0$, $\sigma_{\text{pore}} = \sigma_{\text{NC}} = 2.5\text{Å}$ and r is the shortest distance between each atom and the pore wall.

The pore is defined as a long cylinder of radius r_{pore} with a conical mouth followed by a flat wall perpendicular to the axis of the pore (Fig. 1). Due to the excluded volume interaction of the pore, the effective radius of the pore is $(r_{\text{pore}} - \sigma_{\text{pore}})$. This pore geometry is consistent with the observed geometry (29) of the solid state nanopores used in the experimental study of tRNA (12).

Simulation details

Umbrella sampling (30) was used in conjunction with replica exchange protocols (31, 32) to calculate the free energy as a function of tRNA position. Each umbrella was included as a harmonic restraint along Γ (coordinate of the center of mass of 41 residues that are near the anti-codon stem loop; Fig. 1). Umbrellas were defined from Γ =-18 nm to Γ =10 nm spaced at 0.2 nm intervals. Initially, short equilibration simulations were iteratively performed: The model was initially equilibrated at $\Gamma=-3$ nm. The equilibrated structure was then used to initiate the $\Gamma=-2.8$ nm and the $\Gamma=-3.2$ nm runs. This was repeated until $\Gamma = 10$ nm (inside the pore) and $\Gamma = -18.0$ nm (outside the pore) were reached. The system was initially positioned, such that the ASL loop was inserted in the pore. After an initial equilibration period, replica exchange simulations with 10 temperatures were performed for each value of the umbrella position. No electrophoretic bias was applied during the simulations. These simulations were repeated for pores of radii 3.5nm, 3.8nm and 4nm for tRNA arg and tRNA lle. The simulations were performed using Gromacs (v4.6.7) (33) with in-house source-code modifications added to include the poretRNA interactions. Reduced units were utilized for all calculations. The iterative equilibration runs were each performed for 500,000 steps of size 0.002, while the replica exchange runs were performed for at least 80 million steps. Comparison of tRNA dynamics with a SMOG model and an explicit-solvent model suggests the effective reduced timescale is between 50ps and 1 ns (34). Accordingly, one may estimate the effective simulated time of each replica to be approximately 50-100 μ s. For replica exchange simulations, the temperatures between 0.71 and 0.89 were chosen with geometric spacing since it resulted in an exchange acceptance probability of approximately 0.2. Langevin dynamics protocols with a leap-frog integrator were applied to maintain a constant reduced temperature. All reported quantities were obtained for the lowest simulated temperature of 0.71 (reduced units). In this model, the tRNA structure is found to melt at around 0.9 reduced units (not shown). Since tRNA molecules tend to denature around 350K (35), the simulated temperatures may be estimated as ranging from 280 to 350 K.

The Weighted Histogram Analysis Method (WHAM) (36) was used to calculate free-energy profiles from the umbrella simulations. To verify convergence of the free-energy profiles, WHAM calculations were repeated using the first, or second, half of the simulated time (Fig. S1 in the Supporting Material) To account for the electrophoretic bias along the pore, we assume a uniform electric potential gradient that is parallel to the axis of the pore. The electric potential decreases linearly from $V_{applied}$ to zero over a distance of 30 nm ($\Gamma=-10$ nm to $\Gamma=20$ nm). To implement a reduced effective charge due to solvation of phosphate groups, each phosphorous atom was modeled as carrying an effective charge of $-\theta_c$, where the precise value in each simulation was held at a specific uniform value. Different simulations used distinct values that ranged from 0 to 1. $\theta_c=1$ would correspond to the case where there is no counter-ion condensation. The average electrophoretic potential energy of the tRNA was calculated *post hoc* as a function of the translocation coordinate (Γ), based on the simulated positions of the P atoms. That is, the electrophoretic potential profile was added to the free-energy profile obtained from WHAM, in order to provide an effective free-energy profile as a function of Γ . Here, directly adding the potential energy is a suitable approximation, since the variation in electric potential energy (for a given value of Γ) was small ($<1~k_BT$), relative to the change in potential energy during translocation ($\approx100~k_BT$).

Results and Discussion

In order to identify the molecular factors that lead to differential kinetics of tRNA translocation through nanopores, we constructed a simplified energetic model and then used MD simulations to calculate the free-energy barriers associated with tRNA translocation events. Specifically, we utilized an all-atom structure-based model (24, 25), where all interactions were explicitly defined to stabilize an experimentally-resolved structure. This model was chosen since it provides a description of molecular flexibility that is consistent with more highly-detailed models (37) and crystallographic B-factors (38). To model the presence of the nanopore, we introduced repulsive interactions between the tRNA and pore, where the pore was described as a cylindrical surface with a conical opening (Fig. 1). By defining the tRNA-pore interactions as purely repulsive, this model is designed to identify the extent to which confinement of tRNA leads to specific structural deformations during translocation. That is, since the model provides a description of flexibility that is consistent with other theoretical and experimental measures, the objective when applying this model is to determine whether molecular flexibility is sufficient to rationalize the translocation kinetics. As described below, we find that flexibility is not sufficient, and more dramatic unfolding processes are likely to occur. Since the modeled flexibility and sterics of confinement are consistent with more highly-detailed models, one further expects that partial unfolding will be a robust feature when using other models. In order to assess whether the predicted kinetics are quantitatively consistent with experimental measurements, we used perturbation techniques to describe the effects of electrophoretic bias, counter-ion condensation and hydrodynamic drag. When accounting for these factors, the simplified representation of the tRNA-pore energetics is sufficient to rationalize the differential translocation kinetics of tRNA^{Ile} and

Biophysical Journal 00(00) 1-12

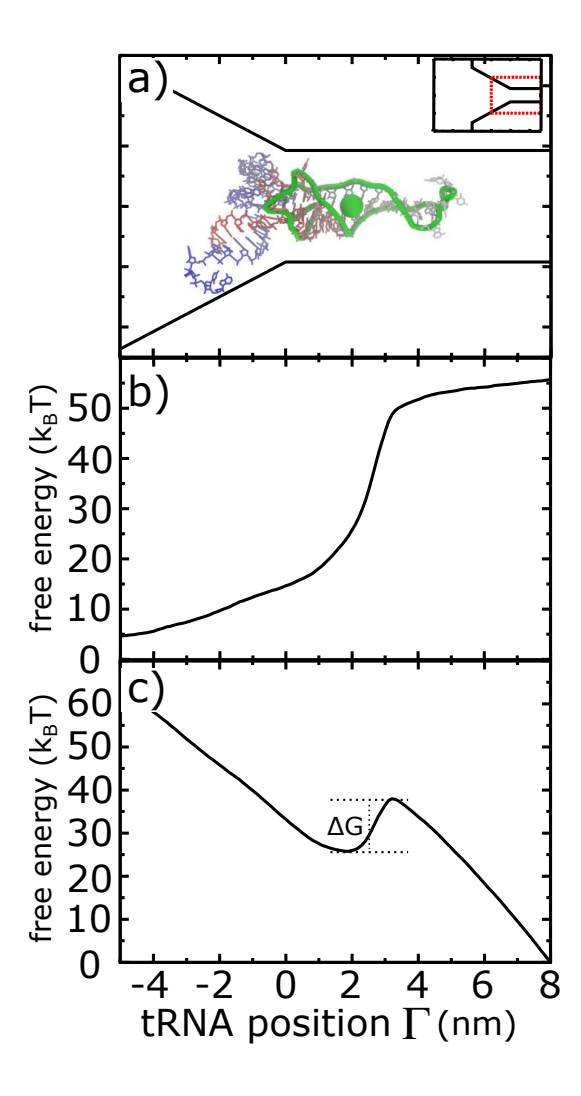


Figure 2: Modeled pore geometry and calculated free-energy profiles. a) Schematic representation of a 3.7 nm diameter pore (full pore dimensions shown in inset). tRNA are is shown to scale. Here, translocation through the pore is described by the coordinate Γ : axial position of the center of mass of residues near the anticodon stem-loop (ASL) region. The ASL region used for center-of-mass calculations is shown in green tubes, and the position of the center of mass is depicted by a green sphere. b) Free-energy profile in the absence of an applied electric field. As expected, there is a large (> $50k_BT$) barrier, which is consistent with a lack of observed translocation events in the absence of an applied field (39). c) Free-energy profile obtained after including the effect of an external potential of strength 200mV. Under these conditions, the predicted free-energy barrier ΔG is approximately $12k_BT$.

tRNA^{Arg}. From a mechanistic perspective, these calculations implicate partial unfolding as the key molecular process that determines translocation kinetics.

Simplified molecular model captures translocation kinetics

To determine whether the simplified model is able to account for differential tRNA kinetics, we first calculated the free-energy barriers of translocation in the absence of an electrophoretic bias. After calculating the field-free barriers, we then introduced electrophoretic effects to calculate perturbed free-energy surfaces. To illustrate the overall approach, we first provide a description for tRNA^{Arg}. In the simulations, intramolecular tRNA interactions are explicitly defined to stabilize the folded conformation, whereas the tRNA and pore only interact through a repulsive potential. It should be noted that nitride pores can form non-specific stabilizing interactions with tRNA, which can introduce an overall drag on the molecule (40, 41).

As described below, in the current study, we account for drag implicitly using a perturbative approach. Umbrella sampling and replica exchange techniques were applied to calculate the free energy as a function of tRNA position within the pore (see Methods for simulation details). The corresponding rates of pore translocation were then obtained by describing tRNA motion in terms of diffusion along a one-dimensional free-energy surface. Specifically, we calculated the free energy as a function of the axial position (Γ) of the anticodon stem loop (Fig. 2a, green). By describing the motion in terms of diffusion across a one-dimensional free-energy surface $G(\Gamma)$, the corresponding mean first passage time (MFPT) may be calculated according to (42, 43):

$$MFPT = \int_{\Gamma_{\text{init}}}^{\Gamma_{\text{f}}} d\Gamma \int_{-\infty}^{\Gamma} d\Gamma' \frac{\exp[(G(\Gamma) - G(\Gamma'))/k_B T]}{D_{\Gamma}^{\text{eff}}(\Gamma')},$$
(5)

where $\Gamma_{\rm init}$ corresponds to the position of the free-energy minimum that is encountered immediately before crossing the barrier (i.e. post-capture, pre-translocation) and $\Gamma_{\rm f}$ corresponds to the value of the same coordinate when the entire molecule is inside the pore. Numerically, $\Gamma_{\rm init} \approx 2 {\rm nm}$ and $\Gamma_{\rm f} = 7 {\rm nm}$ (Fig. 2). While it is possible that the diffusion of tRNA molecules in nanopores will be position-dependent, as observed in protein folding studies (44), for simplicity we apply a constant value based on Stokes-Einstein estimates $(100 \mu m^2/s)$ for a radius of gyration of $\sim 2.3 {\rm nm}$). Consistent with this estimate, proteins of similar radii of gyration have been observed to show comparable diffusion constants in vitro (45, 46).

As expected, in the absence of an electric field there is a large ($> 50k_BT$) free-energy barrier (Fig. 2b). A barrier of this magnitude would correspond to negligibly slow kinetics, which is consistent with a lack of observed translocation events in the absence of a significant electrophoretic bias (39).

To calculate the rate of translocation as a function of applied field strength, we used our field-free simulations and employed a perturbation approach. The average electrostatic potential energy was calculated as a function of the progress coordinate Γ and then added to the unperturbed free-energy profile. For these calculations, the field was modeled as being uniform strength between the openings of the conical mouth of the pore, and each backbone phosphorous atom was assigned a charge of -e. Intra-tRNA electrostatic interactions were not considered, since these are implicitly described in structure-based models (47). To account for the influence of counterion condensation and drag on the tRNA, we further rescaled the effective charge of each residue by the factor θ_c . While an exact value of θ_c is not currently known, direct force measurements have estimated it to be approximately 0.25-0.35 for double stranded DNA in the presence of a nanopore (48). However, it is worth noting that Ghosal (49) showed the effective rescaling of electrophoretic forces may primarily arise from hydrodynamic drag effects. Luan et al. (40, 41) came to the same conclusion by observing a pore size dependence on the radial ion distribution in molecular dynamics simulations. In the current study, we do not distinguish between these possible contributions. Rather, we use these empirical measurements and predicted values to guide the approximate scale of θ_c in our calculations. For values of θ_c ranging from 0.25 to 0.40, we added the effective electrostatic energy to the unbiased free energy profile, in order to estimate the field-dependent free-energy profile along Γ .

Consistent with experimental observations, we find that the free-energy barrier and mean first passage times (MFPT) decrease with increasing electrophoretic bias (Fig. 3). At low field strengths, the MFPT decreases with electrophoretic bias. However, at high applied voltages, the scale of the electrophoretic bias greatly exceeds the sterically-induced barrier, which leads to a downhill free-energy profile (Fig. S2). As a result, the MFPT becomes saturated and appears to adopt a diffusion-limited value.

While the presented model provides a simplified representation of the system, the predicted kinetics are on the same scale as those obtained experimentally (12) (Fig. 3). When accounting for the uncertainty in the condensation factor θ_c , the predicted range of rates includes the experimental values for applied voltage that span from 200-400 mV, for both tRNA^{Arg} and tRNA^{Ile}. We also find that tRNA^{Phe} is slower than tRNA^{Ile} (Figs. S3 and S4). The displayed level of agreement indicates that native interactions and excluded volume effects are sufficient to provide a rough estimate of the translocation rates. It is also interesting that the free-energy barriers reported here are similar to the predicted internal energy of tRNA^{Phe} bending (50), which was based on an adiabatic mapping technique. While the range of predicted timescales is somewhat broad, the uncertainty in θ_c only introduces an uncertainty of $\pm 5k_BT$ in the free-energy barrier height. When considering the various unquantified experimental factors (pore asymmetry, non-uniform field effects, etc), it is non-trivial to obtain barriers that are consistent with experiments to within a few k_BT . This degree of similarity is even more surprising when one considers that the effective free-energy profiles result from the contributions of multiple large ($\sim 50 - 100k_BT$) quantities (i.e. initial free-energy barrier and electrophoretic effects). If the molecular model, or the modeled electrophoretic effects, were sufficiently imprecise, then the predicted timescales could easily differ from experiments by many orders of magnitude. Here, we consider the case where the tRNA anticodon region enters the pore first. This simplification is motivated by the observation that the flexibility of the 3'-CCA is much larger than that of the anticodon region, as measured by the RMSF (Fig. S5). Accordingly,

¹linearly decreasing from the value V_{applied} to zero over a distance of 30 nm along the axis of the pore

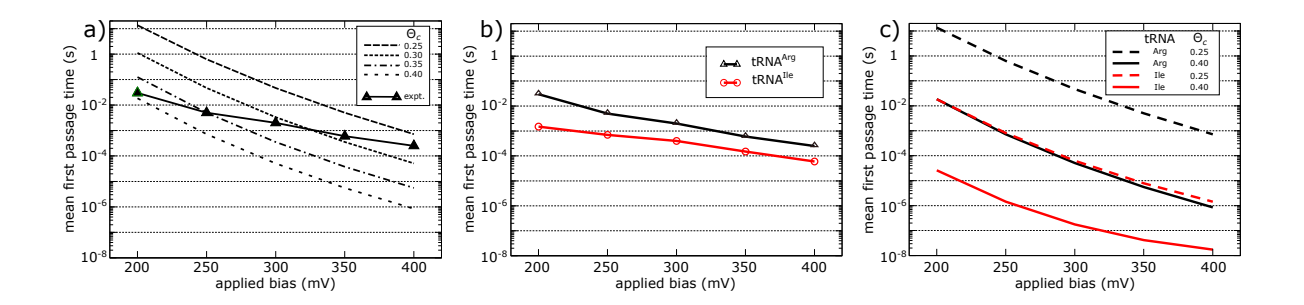


Figure 3: Predicted mean first passage times (MFPT) are comparable to experimental dwell times. a) MFPT predicted for tRNA^{Arg} as a function of applied field strength for different values of the ion condensation factor θ_c (dashed lines). The experimentally-measured dwell times are within the range of predicted values, which illustrates how a simple energetic model can predict an overall timescale that is consistent with experimental measurements. b) Experimental dwell times for tRNA^{Arg} and tRNA^{Ile} show a distinct separation, where shorter dwell times are associated with tRNA^{Ile}. This separation in timescales is consistent with previous experimental measurements (12). Here, to reduce the influence of pore heterogeneity, measurements were taken for both species using the same physical pore. c) Theoretical MFPT for tRNA^{Arg} and tRNA^{Ile} ($\theta_c = 0.25$ and 0.40 shown) also predict faster kinetics are associated with tRNA^{Ile}. Overall, the structure-based model identifies differential kinetics and timescales that are similar to experiments.

this difference in flexibility should disfavor initial capture of the 3'-CCA end. While it is possible that the tRNA may enter via the 3'-CCA end, the current study shows that capture via the anticodon region is sufficient to rationalize the experimental differences in rates. However, it is worth noting that, since the in-pore ensemble was exhaustively sampled, the structural properties of the tRNA inside of the pore (described below) will not depend on the direction of entry. With these limitations in mind, the current comparison indicates that the model provides a physical-chemical description of the mechanical properties of tRNA that is consistent with experimentally-measured kinetics.

In addition to providing a predicted translocation timescale for tRNA arg that is similar to experimental values, this model also predicts faster rates for tRNA le (Fig. 3c). The predicted rates for tRNA arg are consistently lower than for tRNA regardless of the precise pore size used in the calculations (Fig. S6). Further, we find that the separation of rates is robust to changes in the simulated temperature (Fig. S7). The robustness of these trends supports the use of simplified structure-based models to identify mechanistic features that can rationalize experimentally observed differences in kinetics.

Partial unfolding of the tRNA is associated with translocation

One can envision a variety of mechanistic scenarios that could explain the apparent free-energy barriers associated with translocation. Translocation could involve bending/shearing motions that allow the molecule to preserve the majority of the secondary and tertiary interactions. A more drastic process could involve loss of some/all tertiary and/or secondary structure interactions. This would result in an unfolded chain that exhibits significant disorder in the backbone. However, pore-induced confinement should disfavor an extended unfolded ensemble (51–54). With this range of mechanistic possibilities, simulations provide an opportunity to identify which of these exhibit physical-chemical properties that are compatible with experimentally-measured kinetics.

To probe whether unfolding/melting is associated with translocation, we calculated the fraction of native contacts formed per residue (Q_i) as a function of the translocation coordinate Γ . Here, native contacts are defined as non-bonded interactions present in the native structure of the tRNA, as identified by the Shadow algorithm (55). Consistent with studies of protein folding, for a given simulated configuration, a native contact is considered to be "formed" if the respective atom pair is within 1.2 times the native distance (24, 25, 56). We further partition the native contacts into stacking and non-stacking (e.g. base pairing and tertiary) interactions. We find that the average fraction of non-stacking native interactions decreases as the tRNA molecule enters the pore (Figs. 4a,c). Specifically, there is a decrease in the fraction of contacts formed in the acceptor arm region (residues 1-7, 50, 66-73; Fig. S8) at $\Gamma \approx 2-3$ nm. There is also a concomitant decrease in the fraction of stacking contact pairs in these residues (Fig. S9). The remaining residues do not display a significant reduction in Q_i , indicating that overcoming the free-energy barrier is primarily associated with changes in the acceptor stem.

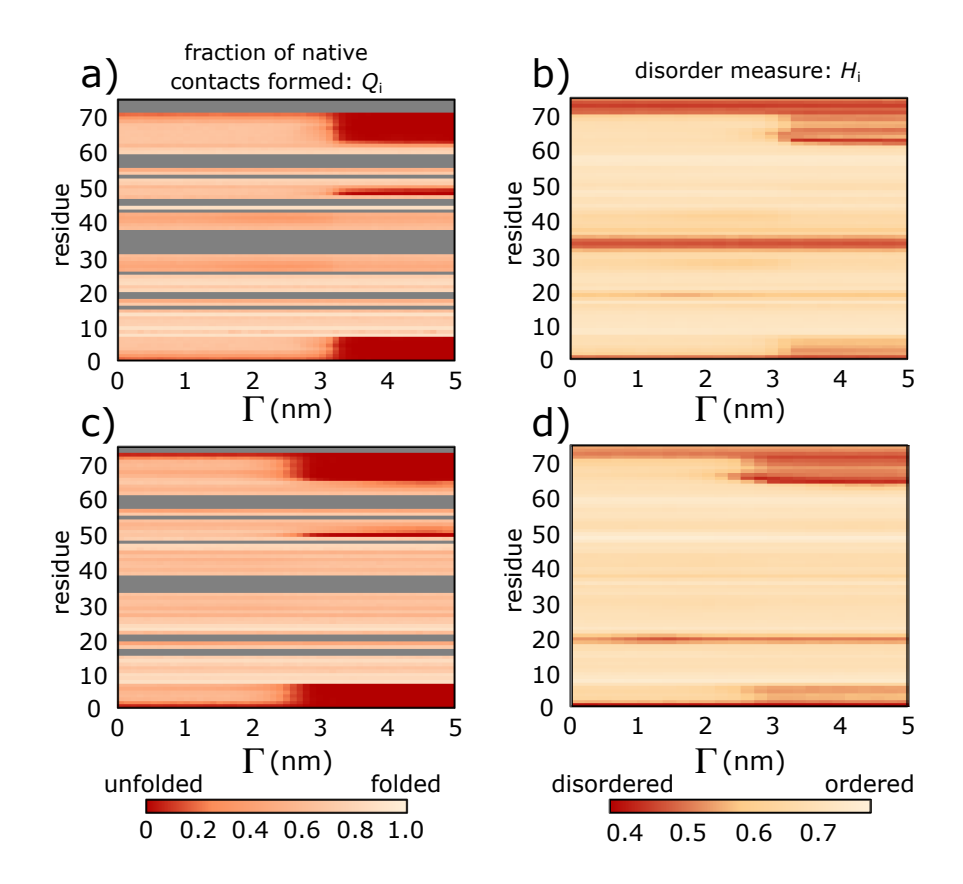


Figure 4: Pore entry leads to tRNA unfolding. a) Fraction of native contacts formed per residue Q_i , as a function of tRNA translocation, for tRNA^{Arg}. Gray indicates that a residue does not have any contacts in the native structure. As the tRNA molecule initially enters the pore ($\Gamma \sim 3$ nm), there is a sharp decrease in the fraction of native contacts formed (~ 0.9 to ~ 0.2) in the acceptor arm and CCA end (Fig. 1). b) Average Hellinger distance per residue (H_i), as a function of translocation coordinate Γ , for tRNA^{Arg}. There is an abrupt decrease in H_i (from ~ 0.7 to ~ 0.4) for acceptor arm residues, which signifies an increase in disorder of the tRNA backbone. Similarly, Q_i and H_i calculated for tRNA^{Ile} (panels c, d) confirm a decrease in native content and increase in disorder are associated with nanopore translocation for both molecules.

Since the loss of native structure would suggest the tRNA molecule unfolds upon entry into the pore, we next asked whether there is also a substantial increase in the degree of disorder of the molecule. To address this, we calculated the Hellinger distance between the distribution of each backbone dihedral angle and a uniform distribution. The Hellinger distance is a measure of similarity between two probability distributions, and it is defined as (57):

$$H = \frac{1}{\sqrt{2}} \sqrt{\sum_{j=1}^{k} (\sqrt{p_{j}} - \sqrt{q_{j}})^{2}},$$
(6)

where $P=(p_1,\ldots,p_k)$ and $Q=(q_1,\ldots,q_k)$ are any two discretized and normalized probability distributions. H=0 for identical distributions, and $0 < H \le 1$ if there are differences, where larger values indicate more significant differences in the distributions. Here, we compare the probability distribution of an individual dihedral angle (P) against a uniform distribution (Q). A uniform distribution is used for comparison, since it would represent a perfectly disordered dihedral angle. With this definition, H will be proportional to the degree of order in an individual dihedral. For reference, representative distributions for $H \sim 0.8$ are shown in Figure S11.

We find that upon tRNA entry into the pore, an increase in disorder coincides with a loss of secondary structure (Fig. 4). Specifically, there are sharp decreases in the average value of H for specific residues (H_i : average value of H for dihedrals in a residue) upon entry (Figs. 4b,d). While the RNA backbone is well-ordered prior to entering the pore ($H_i \sim 0.7$ for most residues), the loss of native contacts leads to the tRNA arm becoming locally disordered ($H_i \sim 0.4$), even in this confined environment. These low values of H_i are comparable to the values found for the single-stranded 3'-CCA end (residues 74 to

Biophysical Journal 00(00) 1-12

76), which has previously been described as a highly disordered/unfolded region (58). Together, this analysis reveals that the acceptor arm does not simply deform, but it enters a disordered ensemble of unfolded configurations during the translocation process. With regards to the dynamics of other tRNA types, the current results suggest that if a tRNA molecule favors a larger angle between the acceptor arm and ASL (e.g. mitochondrial tRNA), or if the acceptor arm is less stable, one should observe faster nanopore translocation kinetics.

Unfolding and confinement lead to non-monotonic changes in configurational entropy

One implied consequence of the presented calculations is that capture rates and translocation rates will have opposing temperature dependencies. To better understand the potential temperature dependence, it is instructive to consider the configurational entropy as a function of tRNA displacement. Before discussing the results, it is important to note that these calculations only describe the configurational entropy of the tRNA molecule. Accordingly, one should not compare the precise values to experimental quantities, which will necessarily depend on the solvent. From our simulations, we calculated the configurational entropy as a function of tRNA position (Fig. 5a) from the free energy and average energy according to: $\Delta S(\Gamma) = (\langle \Delta E \rangle(\Gamma) - \Delta G(\Gamma))/T.$ We find that during initial association (i.e. capture) with the pore $(-5 \text{nm} < \Gamma < 0 \text{nm})$, there is a marginal decrease in configurational entropy. This decrease may be largely attributed to the reduction of accessible rotational motion. To quantify the change in rotational motion upon entry into the pore, we calculated the orientational order parameter

$$m = \frac{3\cos^2\theta - 1}{2}. (7)$$

Here, θ is the angle formed by the first principal axis (lowest moment of inertia. Fig. S12) with the pore axis. The average value of m as a function of the translocation coordinate $(\bar{m}(\Gamma))$ displays an increase from ~ 0 (isotropic) to ~ 1 (co-linear) that coincides with a reduction in the configurational entropy (Figs. 5b and S13). The variance of m also decreases as the tRNA approaches the pore, where the distribution of m values is unimodal (not shown). After initial association with the pore $(\Gamma \sim 0)$, the tRNA molecule transiently samples a free-energy minimum (Fig. 2c) prior to unfolding the terminal acceptor arm helix (Figs. 4b,d). As the acceptor arm unfolds, there is a decrease in the average value of H_i (H_i of arm residues decrease from > 0.65 to ~ 0.5 , Figs. 5c and S14²), with individual values dropping by as much as 0.3 (Fig. S14). Together, the modest reduction in entropy during association would suggest that the rate of tRNA capture will be weakly dependent on temperature, where capture rates should decrease with increasing temperature. In contrast, the increase in entropy upon unfolding indicates that translocation rates should increase rapidly with temperature. We also note that the apparent change in configurational entropy is different for the two tRNA species (Fig. 5a). This may be attributed to differences in stability of the acceptor arm helix when using this model. Specifically, since the root mean squared fluctuations (RMSF) of the acceptor arm helix is larger for tRNA^{Ile} than tRNA^{Arg} when the molecules are folded (Fig. S5), there should be a smaller increase in entropy upon unfolding for tRNA^{Ile}. This differential degree of flexibility is also supported by crystallographic B-factors, which implicate larger RMSF values for tRNA Ile (1.38 Å) than tRNA Arg (0.86 Å). Together, these observations demonstrate that the predicted temperature effects on translocation kinetics are generally in agreement with independent experimental observations.

Conclusion

Nanofabrication technologies continue to be developed as a staggering rate. With the many possibilities for novel nanodevices, there is a growing need for quantitative descriptions of the underlying molecular processes that are being exploited. In the current study, we demonstrate how a relatively simple molecular model may be used to explore the origins of differential timescales of biomolecular transport through a nanopore. We find that tRNA transport is likely associated with partial unfolding/melting of the tRNA structure. This suggests new strategies for designing nanotechnologies that can precisely measure the mechanical properties of individual biomolecules. Through the iterative development of theoretical models and experimental devices, it should soon be possible to design a range of nanotechnologies that can report on the precise properties of arbitrarily-complex molecular systems.

Author contributions

P.B. performed all production simulations. H.Y. performed preliminary simulations. R.H. discussed results and analysis. All author prepared the manuscript.

²tRNA^{Arg}: residues 3-6, 66-69; tRNA^{Ile}: residues 1-4, 65-68

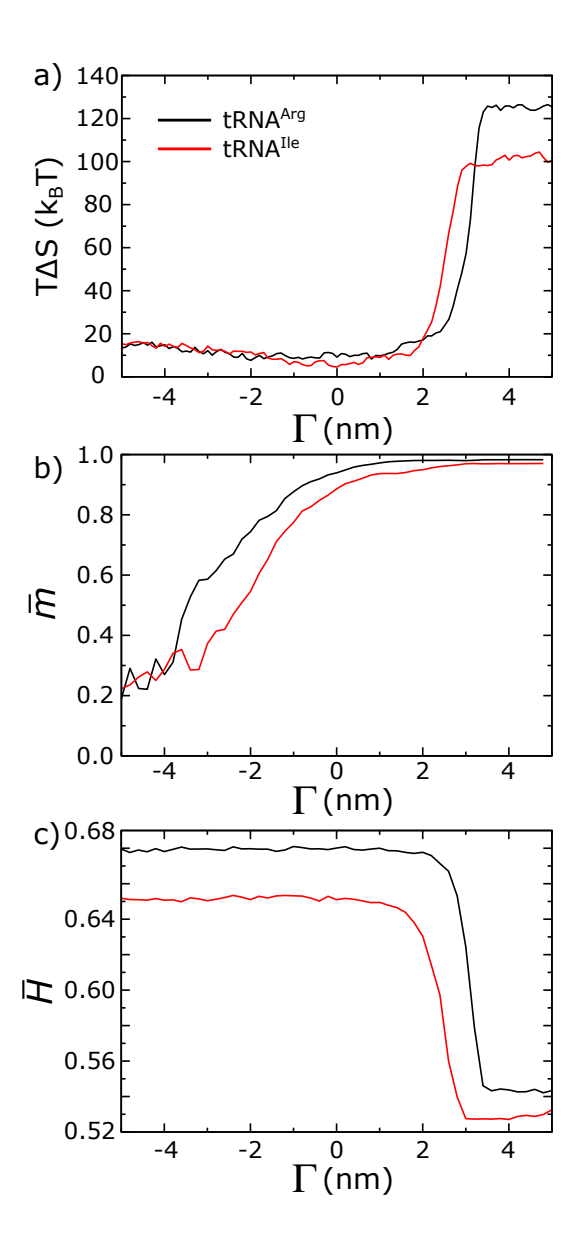


Figure 5: Non-monotonic configurational entropy during translocation. a) During initial association with the pore ($\Gamma < 0$), there is a modest decrease in configurational entropy, which is followed by a sharp increase during translocation ($\Gamma > 0$). b) The initial decrease in configurational entropy may be partially attributed to the reduction in accessible rotational motion, as measured by the orientational order parameter \bar{m} . c) During translocation, the overall increase in biomolecular disorder, as measured by the average value of H for acceptor arm residues (\bar{H}) can rationalize the sharp increase in configurational entropy. This overall non-monotonic behavior of ΔS suggests that tRNA capture and translocation will have opposing dependencies on temperature.

Acknowledgments

We would like to thank the Northeastern University Research Computing team and the Discovery Cluster for computational support. This work was supported by a National Science Foundation (grant Nos. MCB-1350312, MCB-1915843 and MCB-1645671).

SUPPLEMENTARY MATERIAL

An online supplement to this article can be found by visiting BJ Online at http://www.biophysj.org.

Biophysical Journal 00(00) 1-12

References

- 1. Dekker, C., 2007. Solid-state nanopores. Nat. Nanotech. 2:209.
- 2. Venkatesan, B. M., and R. Bashir, 2011. Nanopore sensors for nucleic acid analysis. Nat. Nanotech. 6:615.
- 3. Miles, B. N., A. P. Ivanov, K. A. Wilson, F. Doğan, D. Japrung, and J. B. Edel, 2013. Single molecule sensing with solid-state nanopores: Novel materials, methods, and applications. Chem. Soc. Rev. 42:15–28.
- 4. Spitzberg, J. D., A. Zrehen, X. F. van Kooten, and A. Meller, 2019. Plasmonic-Nanopore Biosensors for Superior Single-Molecule Detection. Advanced Materials 31:1–18.
- 5. Danda, G., and M. Drndić, 2019. Two-dimensional nanopores and nanoporous membranes for ion and molecule transport. Curr. Opin. Biotech. 55:124–133.
- 6. Cressiot, B., A. Oukhaled, G. Patriarche, M. Pastoriza-Gallego, J. M. Betton, L. Auvray, M. Muthukumar, L. Bacri, and J. Pelta, 2012. Protein transport through a narrow solid-state nanopore at high voltage: Experiments and theory. ACS Nano 6:6236–6243.
- 7. Yusko, E. C., J. M. Johnson, S. Majd, P. Prangkio, R. C. Rollings, J. Li, J. Yang, and M. Mayer, 2011. Controlling protein translocation through nanopores with bio-inspired fluid walls. Nat. Nanotech. 6:253.
- 8. Larkin, J., R. Y. Henley, M. Muthukumar, J. K. Rosenstein, and M. Wanunu, 2014. High-bandwidth protein analysis using solid-state nanopores. Biophys. J. 106:696–704.
- 9. Waduge, P., R. Hu, P. Bandarkar, H. Yamazaki, B. Cressiot, Q. Zhao, P. C. Whitford, and M. Wanunu, 2017. Nanopore-Based Measurements of Protein Size, Fluctuations, and Conformational Changes. ACS Nano 11:5706–5716.
- Varongchayakul, N., J. Song, A. Meller, and M. W. Grinstaff, 2018. Single-molecule protein sensing in a nanopore: a tutorial. Chem. Soc. Rev. 47:8512–8524.
- 11. Wanunu, M., T. Dadosh, V. Ray, J. Jin, L. McReynolds, and M. Drndić, 2010. Rapid electronic detection of probe-specific microRNAs using thin nanopore sensors. Nat. Nanotech. 5:807.
- 12. Henley, R. Y., B. A. Ashcroft, I. Farrell, B. S. Cooperman, S. M. Lindsay, and M. Wanunu, 2016. Electrophoretic Deformation of Individual Transfer RNA Molecules Reveals Their Identity. Nano Letters 16:138–144.
- 13. Thompson, R. C., and P. J. Stone, 1977. Proofreading of the codon-anticodon interaction on ribosomes. Proc. Natl. Acad. Sci. USA 74:198–202.
- 14. Ruusala, T., M. Ehrenberg, and C. G. Kurland, 1982. Is there proofreading during polypeptide synthesis? EMBO J. 1:741-745.
- Pape, T., W. Wintermeyer, and M. Rodnina, 1999. Induced fit in initial selection and proofreading of aminoacyl-tRNA on the ribosome. EMBO J 18:3800–3807.
- 16. Cochella, L., and R. Green, 2005. An active role for tRNA in decoding beyond codon:anticodon pairing. Science 308:1178-80.
- 17. Yarus, M., M. Valle, and J. Frank, 2003. A twisted tRNA intermediate sets the threshold for decoding. RNA 9:384-5.
- 18. Schmeing, T. M., and V. Ramakrishnan, 2009. What recent ribosome structures have revealed about the mechanism of translation. Nature 461:1234–42.
- 19. Korostelev, A., and H. F. Noller, 2007. The ribosome in focus: new structures bring new insights. Trends Biochem Sci 32:434-41.
- 20. Frank, J., and C. Spahn, 2006. The ribosome and the mechanism of protein synthesis. Rep. Prog. Phys. 69:1383–1417.
- 21. Nguyen, K., and P. C. Whitford, 2016. Steric interactions lead to collective tilting motion in the ribosome during mRNA-tRNA translocation. Nat. Commun. 7:10586–10586.
- Yang, H., J. K. Noel, and P. C. Whitford, 2017. Anisotropic Fluctuations in the Ribosome Determine tRNA Kinetics. J. Phys. Chem. B 121:2777–2786.
- 23. Nguyen, K., H. Yang, and P. C. Whitford, 2017. How the Ribosomal A-Site Finger Can Lead to tRNA Species-Dependent Dynamics. J. Phys. Chem. B 121:2767–2775.
- 24. Whitford, P. C., J. K. Noel, S. Gosavi, A. Schug, K. Y. Sanbonmatsu, and J. N. Onuchic, 2009. An all-atom structure-based potential for proteins: Bridging minimal models with all-atom empirical forcefields. Proteins 75:430–441.
- Noel, J. K., M. Levi, M. Raghunathan, H. Lammert, R. L. Hayes, J. N. Onuchic, and P. C. Whitford, 2016. SMOG 2: A Versatile Software Package for Generating Structure-Based Models. PLoS Comput. Biol. 12:1–14.
- 26. Delagoutte, B., D. Moras, and J. Cavarelli, 2000. tRNA aminoacylation by arginyl-tRNA synthetase: induced conformations during substrates binding. The EMBO Journal 19:5599–5610. http://emboj.embopress.org/content/19/21/5599.
- 27. Silvian, L. F., J. Wang, and T. A. Steitz, 1999. Insights into Editing from an Ile-tRNA Synthetase Structure with tRNAIle and Mupirocin. Science 285:1074–1077. https://science.sciencemag.org/content/285/5430/1074.
- 28. Shi, H., and P. B. Moore, 2000. The crystal structure of yeast phenylalanine tRNA at 1.93 A resolution: a classic structure revisited. RNA 6:1091-1105. http://rnajournal.cshlp.org/content/6/8/1091.abstract.
- 29. Kim, M., M. Wanunu, D. Bell, and A. Meller, 2006. Rapid Fabrication of Uniformly Sized Nanopores and Nanopore Arrays for Parallel DNA Analysis. Advanced Materials 18:3149–3153. http://dx.doi.org/10.1002/adma.200601191.
- 30. Torrie, G., and J. Valleau, 1977. Nonphysical sampling distributions in Monte Carlo free-energy estimation: Umbrella sampling. J. Chem. Phys. 23:187 199. http://www.sciencedirect.com/science/article/pii/0021999177901218.
- 31. Hukushima, K., and K. Nemoto, 1996. Exchange Monte Carlo Method and Application to Spin Glass Simulations. J. Phys. Soc. Japan 65:1604–1608. https://doi.org/10.1143/JPSJ.65.1604.
- 32. Sugita, Y., and Y. Okamoto, 1999. Replica-exchange molecular dynamics method for protein folding. Chem Phys Lett 314:141–151.
- 33. Hess, B., C. Kutzner, D. van der Spoel, and E. Lindahl, 2008. GROMACS 4: Algorithms for Highly Efficient, Load-Balanced, and Scalable Molecular Simulation. J. Chem. Theory Comput. 4:435–447.

34. Yang, H., P. Bandarkar, R. Horne, V. B. Leite, J. Chahine, and P. C. Whitford, 2019. Diffusion of tRNA inside the ribosome is position-dependent. J. Chem. Phys. 151. https://doi.org/10.1063/1.5113814.

- 35. Crothers, D., P. Cole, C. Hilbers, and R. Shulman, 1974. The molecular mechanism of thermal unfolding of Escherichia coli formylmethionine transfer RNA. Journal of Molecular Biology 87:63 88. http://www.sciencedirect.com/science/article/pii/0022283674905609.
- 36. Kumar, S., J. M. Rosenberg, D. Bouzida, R. H. Swendsen, and P. A. Kollman, 1992. THE weighted histogram analysis method for free-energy calculations on biomolecules. I. The method. J. Comp. Chem. 13:1011–1021.
- 37. Jackson, J., K. Nguyen, and P. Whitford, 2015. Exploring the Balance between Folding and Functional Dynamics in Proteins and RNA. Int. J. Mol. Sci. 16:6868–6889.
- 38. Whitford, P. C., P. Geggier, R. B. Altman, S. C. Blanchard, J. N. Onuchic, and K. Y. Sanbonmatsu, 2010. Accommodation of aminoacyl-tRNA into the ribosome involves reversible excursions along multiple pathways. RNA 16:1196–1204.
- 39. Alibakhshi, M. A., J. R. Halman, J. Wilson, A. Aksimentiev, K. A. Afonin, and M. Wanunu, 2017. Picomolar Fingerprinting of Nucleic Acid Nanoparticles Using Solid-State Nanopores. ACS Nano 11:9701–9710.
- 40. Luan, B., and A. Aksimentiev, 2008. Electro-osmotic screening of the DNA charge in a nanopore. Phys. Rev. E 78:021912.
- 41. Luan, B., and A. Aksimentiev, 2010. Control and reversal of the electrophoretic force on DNA in a charged nanopore. J. Phys. Cond. Matt. 22:454123.
- 42. Zwanzig, R., 1988. Diffusion in a rough potential. Proc. Natl. Acad. Sci. USA 85:2029-30.
- 43. Bryngelson, J., and P. Wolynes, 1989. Intermediates And Barrier Crossing In A Random Energy-Model (With Applications To Protein Folding). J Phys Chem-Us 93:6902–6915.
- 44. Hummer, G., 2005. Position-dependent diffusion coefficients and free energies from Bayesian analysis of equilibrium and replica molecular dynamics simulations. New J. Phys. 7:34–34.
- 45. Brune, D., and S. Kim, 1993. Predicting protein diffusion coefficients. Proc. Natl. Acad. Sci. USA 90:3835–3839. https://www.pnas.org/content/90/9/3835.
- 46. Sadovsky, R. G., S. Brielle, D. Kaganovich, and J. L. England, 2017. Measurement of Rapid Protein Diffusion in the Cytoplasm by Photo-Converted Intensity Profile Expansion. Cell Reports 18:2795 2806. http://www.sciencedirect.com/science/article/pii/S2211124717302784.
- 47. Chan, H., Z. Zhang, S. Wallin, and Z. Liu, 2011. Cooperativity, Local-Nonlocal Coupling, and Nonnative Interactions: Principles of Protein Folding from Coarse-Grained Models. Annu. Rev. Phys. Chem. 62:301–326.
- 48. Keyser, U. F., B. N. Koeleman, S. Van Dorp, D. Krapf, R. M. Smeets, S. G. Lemay, N. H. Dekker, and C. Dekker, 2006. Direct force measurements on DNA in a solid-state nanopore. Nature Physics 2:473–477.
- 49. Ghosal, S., 2007. Electrokinetic-flow-induced viscous drag on a tethered DNA inside a nanopore. Phys. Rev. E 76:061916. https://link.aps.org/doi/10.1103/PhysRevE.76.061916.
- 50. Harvey, S. C., and J. A. McCammon, 1981. Intramolecular flexibility in phenylalanine transfer RNA. Nature 294:286–287. https://doi.org/10.1038/294286a0.
- 51. Zhou, H.-X., and K. A. Dill, 2001. Stabilization of Proteins in Confined Spaces. Biochemistry 40:11289–11293. https://doi.org/10.1021/bi0155504, pMID: 11560476.
- 52. Klimov, D. K., D. Newfield, and D. Thirumalai, 2002. Simulations of β-hairpin folding confined to spherical pores using distributed computing. Proc. Natl. Acad. Sci. USA 99:8019–8024. https://www.pnas.org/content/99/12/8019.
- 53. O'Brien, E. P., G. Stan, D. Thirumalai, and B. R. Brooks, 2008. Factors governing helix formation in peptides confined to carbon nanotubes. Nano Lett 8:3702–8. http://pubs.acs.org/doi/abs/10.1021/n18019328.
- 54. Suvlu, D., S. Samaratunga, D. Thirumalai, and J. C. Rasaiah, 2017. Thermodynamics of Helix–Coil Transitions of Polyalanine in Open Carbon Nanotubes. J. Phys. Cond. Mat. 8:494–499.
- 55. Noel, J. K., P. C. Whitford, and J. N. Onuchic, 2012. The Shadow Map: A General Contact Definition for Capturing the Dynamics of Biomolecular Folding and Function. J. Phys. Chem. B 116:8692–8702.
- 56. Clementi, C., H. Nymeyer, and J. Onuchic, 2000. Topological and energetic factors: What determines the structural details of the transition state ensemble and "en-route" intermediates for protein folding? An investigation for small globular proteins. J. Mol. Biol. 298:937–953.
- 57. Hellinger, E., 1909. Neue Begründung der Theorie quadratischer Formen von unendlichvielen Veränderlichen. Journal für die reine und angewandte Mathematik 136:210–271. http://eudml.org/doc/149313.
- 58. Whitford, P. C., and J. N. Onuchic, 2015. What protein folding teaches us about biological function and molecular machines. Curr. Opin. Struct. Biol. 30:57–62.